



CHORUS

This is the accepted manuscript made available via CHORUS. The article has been published as:

Self-Driven Droplet Powered By Active Nematics

Tong Gao and Zhaorui Li

Phys. Rev. Lett. **119**, 108002 — Published 8 September 2017

DOI: [10.1103/PhysRevLett.119.108002](https://doi.org/10.1103/PhysRevLett.119.108002)

Self-Driven Droplet Powered By Active Nematics

Tong Gao^{1,2*} and Zhaorui Li³

¹*Department of Mechanical Engineering,*

²*Department of Computational Mathematics,
Science and Engineering, Michigan State University*

³*Department of Mechanical Engineering,*

Texas A&M University-Corpus Christi

(Dated: August 7, 2017)

Active matter defines a class of far-away-from-equilibrium systems comprising self-driven micro-particles. Their anomalous physical properties could be applied in areas such as mixing or separation, micro-pumps, and self-healing materials. To realize such applications, a thorough understanding of the physical mechanisms as well as the development of methods to manipulate various active systems are required. Using a coarse-grained active liquid crystal model, we designed and investigated a single self-driven droplet which encapsulated a dense suspension comprising non-motile but mobile active particles that generate extensile stresses. We showed that such droplets can be driven into motion and can have tunable mobilities owing to their internal collective motion, which is characterized by induced active flows and motile disclination defects. Furthermore, it was illustrated that the interplay among the internal directional flows, liquid crystalline structures, droplet size, and surface tension resulted in different types of locomotion and rotation.

Active matter systems are far-from-equilibrium systems comprising biological or synthetic microstructures that convert energy from the local environment to mechanical work [1]. In these systems, particle motions effectively exert active stresses upon the ambient liquid, which itself acts as a coupling medium for complex dynamics as multi-particle interactions within the solvent can manifest themselves as large-scale dynamics at the macroscale [2–5]. To take complete advantage of the anomalous properties of active matter (e.g., large-scale induced motion, enhanced diffusion, and energy conversion), it is essential to design biomimetic materials powered by collective motions. For example, fascinating synthetic bio-active fluids arise when dense suspensions of microtubules (MTs) are inter-connected by walking molecular motors to form active polymer networks [7–9]. It has been found that the sliding MTs are hydrodynamically unstable as they effectively exert extensile dipolar stresses upon the liquid, and will thus induce active flows to bend the aligned structures, leading to an active liquid-crystalline phase with motile disclination defects [10–13]. Such hydrodynamic coupling of the nematic-bending deformations with the generation of jet-like active flows is considerably robust, and has been identified as the “power source” of complex active nematic flows.

To effectively control the collective dynamics in various internally-driven systems, it is critical to manipulate the emergent coherent structures. One way of doing this is to tune the suspension concentration and the amount of chemical fuels [7, 14–16]. Alternatively, we can take advantage of the particle interactions, either individually or collectively, with obstacles and geometric boundaries to manipulate the system more directly. By trapping active suspensions (such as Pusher swimmers or Quincke rollers) within the straight and curved boundaries, stable flow patterns, such as unidirectional circulations, travel-

ing waves, density shocks, and rotating vortices, have already been constructed [17–23]. More interestingly, active polar gels under soft confinement by surface tension are able to generate internal flows to break symmetry and drive the whole-body movement [24–26].

In this Letter we construct a coarse-grained liquid crystal model to study how active nematics interact with a deformable interface by encapsulating a concentrated active suspension in a droplet. We show that the interplay between the internal active nematic flows and soft confinement due to surface tension can generate rich drop translation and rotation dynamics. To begin with, we consider rod-like microparticles that elongate through nearly symmetric stretching or growth, such as MT bundles undergoing polarity sorting [7, 9]. The ensemble dynamics can be described through a probability distribution function $\Psi(\mathbf{x}, \mathbf{p}, t)$ that satisfies a Smoluchowski equation [12, 17, 27, 28] $\frac{\partial \Psi}{\partial t} + \nabla \cdot (\dot{\mathbf{x}}\Psi) + \nabla_p \cdot (\dot{\mathbf{p}}\Psi) = 0$, where \mathbf{x} and \mathbf{p} ($|\mathbf{p}| = 1$) represent the rod’s center-of-mass (c.o.m.) position and orientation, respectively; ∇ is a spatial derivative and $\nabla_p = (\mathbf{I} - \mathbf{p}\mathbf{p}) \cdot \partial / \partial \mathbf{p}$ is a surface derivative on the unit sphere. We further assume that the microparticles are non-motile and only advected by fluid flow, which is described by the translational flux: $\dot{\mathbf{x}} = \mathbf{u} - d_T \nabla \ln \Psi$, where \mathbf{u} is the induced local fluid velocity and d_T is the translational diffusion coefficient. In the meantime, these slender particles rotate due to the fluid velocity gradient $\nabla \mathbf{u}$ and the enhanced steric interactions at a finite concentration which can be incorporated into the model by introducing a local mean-field alignment torque resultant from a Maier-Saupe steric potential [12, 13, 30, 31]. Then we extend the classical Jeffery’s orbit [29] and define the rotational flux as: $\dot{\mathbf{p}} = (\mathbf{I} - \mathbf{p}\mathbf{p}) \cdot (\nabla \mathbf{u} + 2\zeta \mathbf{D}) \cdot \mathbf{p} - d_R \nabla_p \ln \Psi$, where the coefficients d_R and ζ respectively characterize the rotational diffusion and the mean-field torque strength. Instead of

solving the Smoluchowski equation directly, we took moment average [27] to derive a coarse-grained equation for the second moment-tensor $\mathbf{D} = \int_p \mathbf{p}\mathbf{p}\Psi d\mathbf{p}$, which is given by:

$$\overset{\nabla}{\mathbf{D}} + 2\mathbf{E} : \mathbf{S} = 4\zeta (\mathbf{D} \cdot \mathbf{D} - \mathbf{D} : \mathbf{S}) + d_T \Delta \mathbf{D} - 4d_R (\mathbf{D} - \frac{\mathbf{I}}{2}) \quad (1)$$

where $\overset{\nabla}{\mathbf{D}} = \frac{\partial \mathbf{D}}{\partial t} + \mathbf{u} \cdot \nabla \mathbf{D} - (\nabla \mathbf{u} \cdot \mathbf{D} + \mathbf{D} \cdot \nabla \mathbf{u}^T)$ is an upper-convected time derivative, $\mathbf{E} = (\nabla \mathbf{u} + \nabla \mathbf{u}^T)/2$ is the rate-of-strain tensor. The fourth-moment tensor $\mathbf{S} = \int_p \mathbf{p}\mathbf{p}\mathbf{p}\mathbf{p}\Psi_B d\mathbf{p}$ is expressed in terms of \mathbf{D} through the so-called Bingham closure by employing an axisymmetric distribution function Ψ_B which arises naturally as describing nematically-ordered steady states due to the balance between the rotational diffusion and the Maier-Saupe alignment torque in the kinetic model [34, 35]. Note that while these active particles cannot self-swim, their elongation or stretching motions effectively exert dipolar stresses upon the liquid, which may eventually lead to large-scale collective dynamics through the basic transitions and instabilities associated with motile suspensions [34].

Next, we consider such a concentrated active suspension being encapsulated in a 2D droplet that is immersed in a Newtonian liquid. The velocity field \mathbf{u} of the entire domain is assumed to be incompressible (i.e., $\nabla \cdot \mathbf{u} = 0$) and can be solved by a forced Stokes equation:

$$\nabla p - \nabla^2 \mathbf{u} = \frac{\sigma \mu}{\epsilon} \nabla c + \nabla \cdot (c \mathbf{\Sigma}). \quad (2)$$

The first forcing term on the right-hand-side is related to the surface tension (with coefficient σ). Here we employed a diffuse interface approach to treat the sharp fluid/fluid interface as continuous variations of a phase function c ($0 \leq c \leq 1$). Then the phase segregation of the two immiscible fluids can be described by a smooth but narrow transition of c across the interface with a small thickness of order ϵ , following a standard Cahn-Hilliard model:

$$\frac{\partial c}{\partial t} + \mathbf{u} \cdot \nabla c = d_c \nabla^2 \mu, \quad (3)$$

where d_c is known as a mobility coefficient and $\mu = c(c-1)(c-\frac{1}{2}) - \epsilon^2 \nabla^2 c$ is a chemical potential that guarantees a smooth variation of c within the interfacial region [36, 37]. The second forcing term drives the internal collective dynamics, due to the extra particle stress which is obtained as a configurational average of the force dipoles exerted by the particles on the fluid, and takes the form $\mathbf{\Sigma} = \alpha \mathbf{D} + \beta \mathbf{S} : \mathbf{E} - 2\zeta \beta (\mathbf{D} \cdot \mathbf{D} - \mathbf{S} : \mathbf{D})$. Here the three terms arise from a permanent dipole due to the extensile stretching motion with the strength coefficient $\alpha < 0$, resistance to the local flow due to particle rigidity (β is a shape factor), and steric interactions, respectively. The reader is referred to more details on the kinetic model, coarse-graining through Bingham closure,

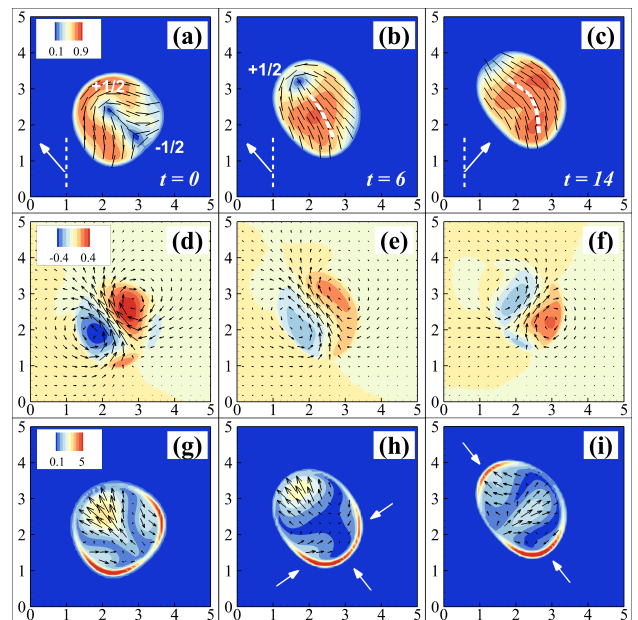


FIG. 1: Sequential snapshots of the dynamics of a Propeller droplet. (a)-(c): the nematic director field superposed on the colormap of the scalar order parameter $0 \leq s(\mathbf{x}, t) \leq 1$ (s is twice the principal eigenvalue of $\mathbf{Q} = \mathbf{D} - \mathbf{I}/2$). The dashed line in the lower left corner represents the averaged propelling direction, while the arrow indicates the instantaneous moving direction of the $+1/2$ defect. (d)-(f): the background fluid velocity vector field superposed upon the colormap of the associated vorticity. (g)-(i): the body-force vector field (i.e., $\mathbf{f} = \nabla \cdot (c \mathbf{\Sigma})$), superposed on its magnitude. The arrows in (h) and (i) represents the contraction directions. The parameters are chosen as $\alpha = -2.0$, $R = 1.25$, $\sigma = 3.0$, $\beta = 0.874$, $\zeta = 0.5$, $d_R = d_T = d_c = 0.05$.

normalization, and parameter choice in the supplementary material [35].

Assuming that the droplet is initially circular with a radius R and carries a suspension that is approximately uniformly isotropic, then we solve the governing equations (1)-(3) in a periodic square domain by using a pseudo-spectral method over long time periods [35]. As shown in Fig. 1, after the initial transient, we captured a quasi-steady self-propelling motion during which the droplet performed swimming strokes as its body periodically wiggles; see movie S1. We refer to this motion as a ‘‘Propeller’’ mode, which is different from the steady-state translation of a mobile cell driven by internal active flows [25, 26], and is instead somewhat reminiscent of the undulating swimming of nematodes [38].

Periodic genesis and continual propagation of $\pm 1/2$ disclination defects were observed during the propelling motion, as highlighted in Fig. 1. In panel(a), the nematic field shows that a pair of $\pm 1/2$ defects, once born, separate from each other along an incipient crack. The $-1/2$ defect quickly vanishes near the interface, while the $+1/2$ defect keeps moving forward. Panel(b) shows

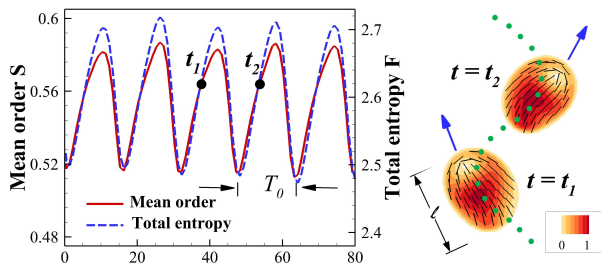


FIG. 2: On the left: mean order and total entropy as a function of time during a propelling motion. On the right: nematic director field superimposed on the colormap of entropy density. The green dotted line represents the c.o.m. trajectory.

that the droplet migrates in the direction of defect motion (marked by the arrow) and elongates into an elliptic shape with a global alignment approximately along the long axis. In the meantime, the body is slightly bent towards the upper right corner (highlighted by the “backbone” marked by a dashed line), which naturally selects the direction of the bending deformation for the next stroke, as marked by the arrow in panel(c). The velocity-vorticity maps in Fig. 1(d)-(f) exhibit an evolution of the internal flow pattern during one stroke. A fluid jet is developed to bend the nematic field lines, “carrying” the propagating $+1/2$ defect with two rolling vortices of opposite signs. The vorticity field is strengthened and weakened through the various stages of the strokes, with the jet direction switching periodically as the Propeller wiggles.

The body force ($\mathbf{f} = \nabla \cdot (c\boldsymbol{\Sigma}))$ distribution in Figs. 1(g)-(i) clearly shows that a net force generation is associated with the motile $+1/2$ defect [12, 13]. Moreover, the confinement effect manifests itself by the generation of a surface tension force across the interface as the droplet bottom contracts (panel(h)), followed shortly thereafter by contractions of both ends of the droplet (panel(i)). Such internal force generation and the accompanying material deformation typically suggest an elastic behavior of the ordered fluid, which can be easily seen in the limit where all the rod-like particles are perfectly aligned. When also neglecting diffusion, the active stress $\boldsymbol{\Sigma}_a = \alpha \mathbf{D}$ follows the evolution equation: $\nabla \cdot \boldsymbol{\Sigma}_a + \frac{2}{\alpha} (\boldsymbol{\Sigma}_a : \mathbf{E}) \boldsymbol{\Sigma}_a = \mathbf{0}$ [35]. Compared with simple neo-Hookean elasticity [39, 40] (i.e., $\nabla \cdot \boldsymbol{\Sigma} = 0$) where the elastic stress can be infinite, the second term here suggests that the nematic elasticity is modulated by flow via a constraint stress due to particle rigidity, which effectively bounds the active stress.

Next, we quantified the internal structure variations and correlate them with the propelling motion. We first define the local entropy density $f(\mathbf{x}, t) = \int_p 2\pi\psi_B \log(2\pi\psi_B) d\mathbf{p}$ by making use of a reconstructed

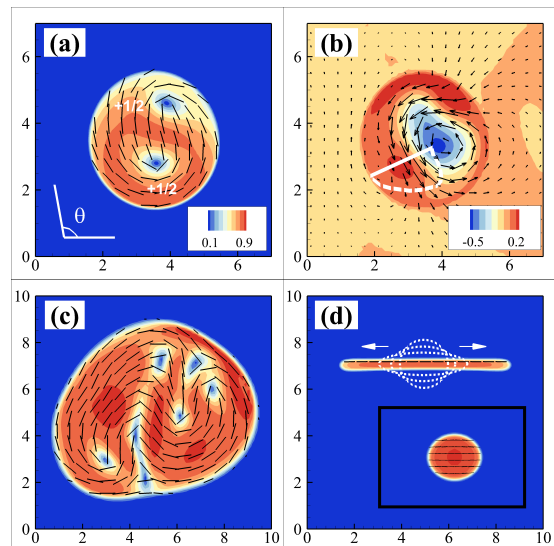


FIG. 3: Active nematic states in relatively large droplets. (a) and (b) show the Rotor’s ($R = 2.0$ and $\sigma = 10.0$) nematic and flow fields, respectively. The angle θ in (a) represents the orientation of the long axis; the dashed line in (b) approximates the velocity profile. (c) The nematic field of a considerably larger droplet that encapsulates multiple defects ($R = 4.0$ and $\sigma = 5.0$). (d) The nematic field of slender ($R = 1.0$ and $\sigma = 0.5$) and thick (inset; $R = 1.0$ and $\sigma = 0.8$) droplets at equilibrium without internal flows. The dashed lines represent the change in shape. The other parameters are chosen as $\alpha = -2.0$, $\zeta = 0.5$, $d_R = d_T = d_c = 0.05$.

distribution function ψ_B through Bingham closure [34, 35], which, as shown on the right in Fig. 2, characterizes the high- and low-order regimes well. Then, the total system entropy can be defined as $F(t) = \int_V f(\mathbf{x}, t) dV$, which fluctuates periodically and varies in phase with the mean order $S(t) = 1/V \int_V s(\mathbf{x}, t) dS$. In this case, the stroke period was measured to be $T_0 \approx 15.0$ during which the $+1/2$ defect approximately travels end-to-end through the droplet’s long axis of length 3.0; while the droplet c.o.m. position moves a distance of about 1.0. Hence we estimate the $+1/2$ defect moves about 3–4 times faster than the Propeller.

Over a wide range of parameters (see an example of phase diagram in Fig. S3 [35]), similar Propeller modes are observed in a narrow regime for relatively small droplets. As the droplet size increases, the internal dynamics quickly switch to become circulatory without generating significant amounts of translation, especially when the interface is less deformable (i.e., with large σ). The motion shown in Figs. 3(a) and (b) is referred to as a “Rotor” mode (see movie S2). A pair of $+1/2$ defects quickly form as the system deviates from its initial isotropic state (panel(a)) and then settles into a quasi-steady rotating motion with a circulating flow (panel(b)), which is very similar to the rotating flow confined in a rigid circular disk [17, 19, 34, 41]. As R increases further,

multiple $+1/2$ defects are generated, and stream inside the droplet, leading to seemingly chaotic internal flows shown in panel(c), as well as random drop movement (see movie S3).

The observed collective motion under soft confinement can be further understood by examining a concatenation of two instabilities (see snapshots in Fig. S4 [35]). Starting from near isotropy, the system spontaneously evolves toward a nematic state. This can be approximately understood by performing a linear stability analysis for an unbounded suspension from which we obtain a maximum growth rate for a long-wave instability at $k = 0$ according to $\lambda_{max} = \frac{\zeta\beta - 2\alpha}{2\beta + 8} + \zeta - 4d_R$ [35]. Note that the isotropic-nematic (I-N) transition is independent of hydrodynamics, and instead due to the inclusion of steric interactions via the Maier-Saupe potential which permits an aligned base-state solution as a balance between the steric alignment torque and rotational diffusion [35]. In 2D, the transition is characterized by a supercritical pitchfork bifurcation occurring at $\zeta \geq 4d_R$ [12, 31].

Immediately after the I-N transition, a bending instability develops from the nematic state [12]. The complex dynamics will then be determined by the interplay between the induced (destabilizing) flow and the (stabilizing) surface tension force. It appears that the droplet must be larger than some emergent nematic structures, such as the $\pm 1/2$ defects and incipient cracks (see theoretical predictions from linear analyses as well as comparisons with numerical simulations in Figs. S5 and S6 [35], respectively) to facilitate the generation of internal nematic flows. Nevertheless, the length scale selection is far more complex when the surface tension coefficient is small, which allows for considerably large droplet deformation or even breakup. As illustrated in Fig. 3(d), when choosing $R = 1.0$ and $\sigma = 0.5$, while being aligned and extending in the x direction, the droplet eventually reaches an equilibrium rod-like shape as the horizontal extension is balanced by the surface tension force at the droplet's two ends. In the meantime, the resultant contraction in the y direction effectively suppresses the instability development. Thus in the regimes with relatively small σ , we can tune the other parameters to construct various stationary shapes without internal flow generation; see Fig. 3(d).

Lastly, we highlight the distinctive features of various modes of droplet motion. As shown in Fig. 4(a), we tracked the c.o.m. trajectories for three typical propelling motions. In this figure, the droplet with a high mobility (red line) has a moderate size and surface tension coefficient. This is because the interfacial elasticity facilitates droplet elongation to comply with the moving jet so that it can travel further during each stroke, leading to an increased amount of translation. Curiously, a Propeller may sometimes “tumble” by making turns (e.g., turning points T_1 and T_2 , see movie S4) after traversing a long distance. It is important to keep in mind that

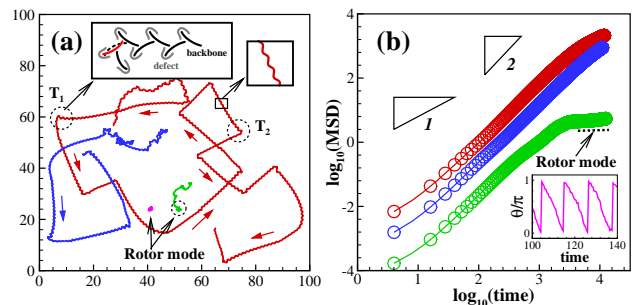


FIG. 4: (a) Typical c.o.m. trajectories of the self-propelling and rotating droplets. The red line corresponds to the case in Fig. 1 with $\sigma = 3.0$ and $R = 1.25$; the blue and green lines represent the cases with a stronger surface tension ($\sigma = 5.0$ and $R = 1.25$) and larger size ($\sigma = 2.0$ and $R = 1.5$), respectively. Top left inset: the backbone position suggests bending in the opposite direction (red solid line) compared with the regular bending (grey dashed line). Top right inset: an enlarged view of the c.o.m. trajectory. (b) MSD. Inset: the Rotor's orientation angle suggests a tumbling motion. The other parameters are chosen as $\alpha = -2.0$, $\zeta = 0.5$, $d_R = d_T = d_c = 0.05$.

a stable propelling motion requires a synchronization of the structure variation, the internal flow development, and the interactions of active nematics and surface tension. The combined effect yields a regular bias in the bending direction during each stroke (see Figs.1(a)-(c)). As illustrated in the top-left inset of Fig. 4(a), a certain degree of mismatch of the internal dynamics near T_1 or T_2 in fact causes the body to bend and then buckle in the “opposite” direction (marked by the red backbone), which effectively flips the c.o.m. trajectory thereafter.

The shape of the Propeller with the higher surface tension (blue line) appears to be more rounded, which means that the jet has a shorter distance to travel; this also reduces control over the swimming direction (for more details, see Fig. S8[35]). It also takes much longer for such a Propeller to settle into a stable stroking motion since irregular turns occur frequently. To examine the propulsive efficiency of the Propellers, we projected their c.o.m. trajectory onto the transverse and the swimming directions whose ratio yields a Strouhal number St . Indeed, the first Propeller (red line) was more efficient at swimming; it had a lower estimated St value of 0.43 compared with 0.67 for the second one (blue line). In addition, when the droplet is relatively large in size (green line), two $+1/2$ defects may occur simultaneously to drive complex internal dynamics, and can even cause a switch from propelling to rotating motion (see movie S5).

The corresponding MSD measurements in panel(b) suggest that the propelling motion can be super-diffusive at relatively long (dimensionless) timescales ($t \sim 10^3$), although it eventually becomes diffusive at even larger timescales. Moreover, we show that a Propeller's mobility can be tuned by orders of magnitude when the

design parameters are appropriately optimized. Conversely, since a Rotor typically does not generate significant translation motions (see trajectory in panel(a) and also movie S2), the MSD (green line/open-circle) may capture interesting mode switches as the drop settles into a steady tumbling motion as measured via the rotation speed of its long axis; see the inset of Fig. 4(b).

We have studied other aspects of the active droplets. For example, we observed that the internal flow strength (characterized by the vorticity and maximum velocity) of Rotors is typically greater than that of Propellers, which is due to the enhanced hydrodynamic interactions between the two $+1/2$ defects. When multiple droplets exist, they coalesce at contact, leading to more frequent mode switching. It would be intriguing to investigate 3D cases in which the topological structures are much more complicated as well as to develop similar models for self-propelling microparticles to incorporate polarity. Furthermore, by combining such models with large-scale discrete particle simulation tools, it may be possible to construct bottom-up multiscale toolkits to facilitate the design and optimization of novel active materials.

Acknowledgement T.G. acknowledges fruitful discussions with M. Shelley, S. Fürthauer, E. Lushi, E. Nazockdast, H. Zhao, and anonymous reviewers' helpful comments. This work is funded by NSF grant DMS-1619960.

* Electronic address: gaotong@egr.msu.edu

- [1] S. Ramaswamy. The mechanics and statistics of active matter. *Ann. Rev. Cond. Matt. Phys.*, 1:323–345, 2010.
- [2] D. Saintillan and M. Shelley. Active suspensions and their nonlinear models. *C. R. Phys.*, 14:497–517, 2013.
- [3] D. Koch and G. Subramanian. Collective hydrodynamics of swimming microorganisms: living fluids. *Annu. Rev. Fluid Mech.*, 43:637–659, 2011.
- [4] M. Marchetti, J. Joanny, S. Ramaswamy, T. Liverpool, J. Prost, M. Rao, and R. Simha. Hydrodynamics of soft active matter. *Rev. Mod. Phys.*, 85:1143–1189, 2013.
- [5] M. Shelley. The dynamics of microtubule/motor-protein assemblies in biology and physics. *Annu. Rev. Fluid Mech.*, accepted.
- [6] S. Köhler, V. Schaller, and A. Bausch. Collective dynamics of active cytoskeletal networks. *PLoS ONE*, 6:e23798, 2011.
- [7] T. Sanchez, D. Chen, S. DeCamp, M. Heymann, and Z. Dogic. Spontaneous motion in hierarchically assembled active matter. *Nature*, 491:431–434, 2012.
- [8] F. Keber, E. Loiseau, T. Sanchez, S. DeCamp, L. Giomi, M. Bowick, M. Marchetti, Z. Dogic, and A. Bausch. Topology and dynamics of active nematic vesicles. *Science*, 345:1135–1139, 2014.
- [9] S. Decamp, G. Redner, A. Baskaran, M. Hagan, and Z. Dogic. Orientational order of motile defects in active nematics. *Nat. Mater.*, 14:1110–1115, 2015.
- [10] S. Thampi, R. Golestanian, and J. Yeomans. Velocity correlations in an active nematic. *Phys. Rev. Lett.*, 111:118101, 2013.
- [11] L. Giomi. Geometry and topology of turbulence in active nematics. *Phys. Rev. X*, 5:031003, 2015.
- [12] T. Gao, R. Blackwell, M. Glaser, M. Betterton, and M. Shelley. Multiscale polar theory of microtubule and motor-protein assemblies. *Phys. Rev. Lett.*, 114:048101, 2015.
- [13] T. Gao, R. Blackwell, M. Glaser, M. Betterton, and M. Shelley. Multiscale modeling and simulation of microtubule/motor protein assemblies. *Phys. Rev. E*, 92:062709, 2015.
- [14] A. Sokolov, I. Aranson, J. Kessler, and R. Goldstein. Concentration dependence of the collective dynamics of swimming bacteria. *Phys. Rev. Lett.*, 98:158102, 2007.
- [15] D. Saintillan and M. Shelley. Emergence of coherent structures and large-scale flows in motile suspensions. *J. R. Soc. Interface*, 9:571–585, 2012.
- [16] G. Henkin, S. J. DeCamp, D. T. N. Chen, T. Sanchez, and Z. Dogic. Tunable dynamics of microtubule-based active isotropic gels. *Phil. Trans. R. Soc. A*, 372(2029), 2014.
- [17] F. Woodhouse and R. Goldstein. Spontaneous circulation of confined active suspensions. *Phys. Rev. Lett.*, 109, 2012.
- [18] M. Ravnik and J. Yeomans. Confined active nematic flow in cylindrical capillaries. *Phys. Rev. Lett.*, 110:026001, 2013.
- [19] H. Wioland, F. Woodhouse, J. Dunkel, J. Kessler, and R. Goldstein. Confinement stabilizes a bacterial suspension into a spiral vortex. *Phys. Rev. Lett.*, 110:268102, 2013.
- [20] A. Bricard, J. Caussin, N. Desreumaux, O. Dauchot, and D. Bartolo. Emergence of macroscopic directed motion in populations of motile colloids. *Nature*, 503:95–98, 2013.
- [21] A. Bricard, J. Caussin, D. Das, C. Savoie, V. Chikkadi, K. Shitara, O. Chepizhko, F. Peruani, D. Saintillan, and D. Bartolo. Emergent vortices in populations of confined colloidal rollers. *Nat. Commun.*, 6:7470, 2015.
- [22] B. Ezhilan and D. Saintillan. Transport of a dilute active suspension in pressure-driven channel flow. *J. Fluid Mech.*, 777:482, 2015.
- [23] A.C.H. Tsang and E. Kanso. Density shock waves in confined microswimmers. *Phys. Rev. Lett.*, 116:048101, 2016.
- [24] S. Thutupalli, R. Seemann, and S. Herminghaus. Swarming behavior of simple model squirmers. *New J. Phys.*, 13:073021, 2011.
- [25] E. Tjhung, D. Marenduzzo, and M. Cates. Spontaneous symmetry breaking in active droplets provides a generic route to motility. *Proc. Natl. Acad. Sci.*, 109:12381–12386, 2012.
- [26] W. Marth, S. Praetorius, and A. Voigt. A mechanism for cell motility by active polar gels. *J. R. Soc. Interface*, 12:20150161, 2015.
- [27] M. Doi and S. Edwards. *The theory of polymer dynamics*, volume 73. Oxford University Press, USA, 1988.
- [28] D. Saintillan and M. Shelley. Instabilities and pattern formation in active particle suspensions: Kinetic theory and continuum simulations. *Phys. Rev. Lett.*, 100:178103, 2008.
- [29] G. Jeffery. The motion of ellipsoidal particles immersed in a viscous fluid. *Proc. Roy. Soc. Lond. Ser. A*, 102:161–179, 1922.
- [30] W. Maier and A. Saupe. Eine einfache molekulare theorie des nematischen kristallinflüssigen zustandes. *Zeit. Nat. Teil A*, 13:564, 1958.

- [31] B. Ezhilan, M. Shelley, and D. Saintillan. Instabilities and nonlinear dynamics of concentrated active suspensions. *Phys. Fluids*, 25:070607, 2013.
- [32] C. Bingham. An antipodally symmetric distribution on the sphere. *Ann. Stat.*, 2:1201–225, 1974.
- [33] J. Feng, C. Chaubal, and L. Leal. Closure approximations for the doi theory: which to use in simulating complex flows of lcps. *J. Rheol.*, 42:1095–1119, 1998.
- [34] T. Gao, M. Betterton, A. Jhang, and M. Shelley. Analytical structure, dynamics, and coarse-graining of a kinetic model of an active fluid. *arXiv:1703.00969*, 2017.
- [35] See supplementary information, which includes Refs.[42–48].
- [36] S. Allen and J. Cahn. A microscopic theory for antiphase boundary motion and its application to antiphase domain coarsening. *Acta Metall.*, 27:1085–1095, 1979.
- [37] D. Anderson, G. McFadden, and A. Wheeler. Diffuse interface methods in fluid mechanics. *Ann. Rev. Fluid Mech.*, 30, 1998.
- [38] X. Shen and P. Arratia. Undulatory swimming in viscoelastic fluids. *Phys. Rev. Lett.*, 106:208101, 2011.
- [39] D. D. Joseph. *Fluid Dynamics of Viscoelastic Liquids*. Applied mathematical sciences, Vol. 84, Springer Verlag, New York, 1990.
- [40] T. Gao, H. H. Hu, and P. Ponte Castañeda. Shape dynamics and rheology of soft elastic particles in a shear flow. *Phys. Rev. Lett.*, 108:058302, 2012.
- [41] K. Kruse, J. F. Joanny, F. Jülicher, J. Prost, and K. Sekimoto. Asters, vortices, and rotating spirals in active gels of polar filaments. *Phys. Rev. Lett.*, 92:078101, 2004.
- [42] C. Hohenegger and M. Shelley. *Dynamics of complex biofluids*. Oxford University Press, 2011.
- [43] D. Saintillan and M. Shelley. Instabilities, pattern formation, and mixing in active suspensions. *Phys. Fluids*, 20:123304, 2008.
- [44] E. Hinch and L. Leal. Constitutive equations in suspension mechanics. part 2. approximate forms for a suspension of rigid particles affected by brownian rotations. *J. Fluid Mech.*, 76:187–208, 1976.
- [45] M. Davies Wykes, J. Palacci, T. Adachi, L. Ristroph, X. Zhong, M. Ward, J. Zhang, and M. Shelley. Dynamic self-assembly of microscale rotors and swimmers. *Soft Matter*, 12:4584–4589, 2016.
- [46] C. Chaubal and L. Leal. A closure approximation for liquid-crystalline polymer models based on parametric density estimation. *J. Rheol.*, 42:177–201, 1998.
- [47] E. Bertin, M. Droz, and G. Grégoire. Boltzmann and hydrodynamic description for self-propelled particles. *Phys. Rev. E*, 74:022101, 2006.
- [48] A. Baskaran and M. C. Marchetti. Statistical mechanics and hydrodynamics of bacterial suspensions. *Proceedings of the National Academy of Sciences*, 106:15567–15572, 2009.